JOURNAL OF SOLID STATE CHEMISTRY **130,** 254–265 (1997)
ARTICLE NO. SC977300

LMTO Band Structure Calculations of $ThCr_2Si_2$-Type Transition Metal Compounds

Dirk Johrendt,*,†,[1] Claudia Felser,*,‡ Ove Jepsen,‡ Ole Krogh Andersen,‡ Albrecht Mewis,† and Jean Rouxel*

*Institut des Matériaux de Nantes, Laboratoire de Chimie des Solides, 2, rue de la Houssinière, 44072 Nantes cedex 03, France;
†Institut für Anorganische Chemie und Strukturchemie II, der Heinrich-Heine-Universität, Universitätsstrasse 1, 40225 Düsseldorf, Germany; and
‡Max Planck Institut für Festkörperforschung, Heisenbergstrasse 1, 70569 Stuttgart, Germany

Received July 29, 1996; in revised form January 22, 1997; accepted January 30, 1997

The electronic structures of $ThCr_2Si_2$-type compounds were studied by means of self-consistent LMTO band structure calculations. Different bonding interactions in $SrRh_2P_2$ are analyzed and their dependence on the electron count are discussed in terms of the formal substitution of elements. The overall bonding situation can be characterized as an interplay between covalent, metallic, and ionic interactions, although metal–metal bonding plays an important role. Particularly, the evolution of the interlayer bonding between the nonmetal atoms by changing the transition metal is examined in more detail. It turns out that the shortening of the interlayer bonds by filling the *d* shell of the transition metal is due to an increasing occupation of nonmetal bonding states which are pushed up to the vicinity of the Fermi level by antibonding metal–nonmetal interactions. The band structures of superconducting $LuNi_2B_2C$ and nonsuperconducting $SrRh_2P_2$ are compared and their similarities are pointed out. A van Hove singularity, generated by metal–metal interaction, coincides with the Fermi level in $LuNi_2B_2C$ and lies about 0.2 eV higher in $SrRh_2P_2$. By doping, it should be possible to induce superconductivity in $SrRh_2P_2$ and related compounds. © 1997 Academic Press

INTRODUCTION

Since the first report of the $ThCr_2Si_2$ type by Ban and Sikirica in 1965 (1), more than 700 compounds have been found to adopt this structure (2). This is the highest number of representatives for any crystal structure. In the formulation AM_2X_2, A generally corresponds to an alkaline earth or a lanthanide element, M is a transition metal, and X an element from groups 3*b*–6*b*. Within the $ThCr_2Si_2$-type family, remarkable discrepancies exist regarding the bonding situation (3). Furthermore, a great variety of interesting physical properties has been observed such as valence fluctuations and mixed valency in $EuNi_2P_2$ (4) and $EuCu_2Si_2$ (5), heavy fermion behavior in $CeCu_2Si_2$ (6) as well as a wide range of magnetic properties (7–10). Superconductivity at low temperatures was reported for several compounds, e.g., in $LaRu_2P_2$ with $T_c = 4.1$ K (11). On the other hand, the discovery of superconducting transition temperatures up to 23 K in Ni-, Pd-, and Pt-based $ThCr_2Si_2$ type borocarbides (12–14) has raised the question of whether or not these materials constitute a new class of high temperature superconductors. Therefore, the electronic structures of these materials have been intensively studied (15–17), whereas investigations of the basic $ThCr_2Si_2$ type are scarce and confined to calculations using the Extended Hückel Method (21–23).

The aim of this paper is to draw a picture of the electronic structure of the $ThCr_2Si_2$-type compounds, based on first principles LMTO band calculations in order to achieve a better understanding of bonding and physical properties. In the face of the high number of compounds and for the sake of clarity, the present analysis has been confined to phosphides. With 50 representatives they are a substantial group within the $ThCr_2Si_2$ family and at long last we have some experience with these materials. Nevertheless the results are basically valid for other X components, i.e., for the silicides, germanides, and borides.

First, we describe the main features of the $ThCr_2Si_2$-type band structure, regarding the different types of interactions, i.e., the M–X, M–M, and X–X bonding. The ARh_2P_2 (A = Ca, Sr) system has been chosen as an example because it presents compounds with long and short P–P distances, depending on the A component. Furthermore, $SrRh_2P_2$ is a candidate for interesting physical properties, as discussed later. The dependence of the bonding on substitution of the A and M components is then studied. In order to see only the electronic effect, the band structures of "$LaRh_2P_2$," "KRh_2P_2," "$SrRu_2P_2$," and "$SrPd_2P_2$" using the geometry of $SrRh_2P_2$ have been calculated (the quotes indicate that

[1] To whom correspondence should be addressed.

0022-4596/97 $25.00

the compounds exist in the $ThCr_2Si_2$ structure, but with slightly different parameters).[2] To investigate the striking evolution of the interlayer X–X distances as a function of the transition metal, we discuss the band structure of $CuRu_2P_2$ and substitute Ru by Rh and Pd, respectively.

In the third part of this paper we turn to the possibility of superconductivity in $ThCr_2Si_2$ phosphide compounds. For this we develop the main important properties of the electronic structure of superconducting $LuNi_2B_2C$ and contrast them with nonsuperconducting $SrRh_2P_2$ within the framework of the van Hove Singularity (vHS) scenario (25).

Crystal Structure

The tetragonal body-centered $ThCr_2Si_2$ structure (space group $I4/mmm$, Fig. 1) is mainly characterized by layers of edge-sharing MX_4 tetrahedra parallel to the xy plane, separated by planes of the base metal atoms (A). The atomic distances within the $^2_\infty[MX_{4/4}]$ layers are found to be slightly smaller than the sum of the covalent radii (indicating strong M–X bonding within the layers), whereas the interlayer distances between the X atoms show a great variety of values. The $ThCr_2Si_2$ type is frequently described as an ordered ternary variant of the $BaAl_4$ structure, which is somewhat unreasonable regarding the representatives with interlayer X–X distances of more than 3 Å. In fact, we have two different branches of this structure type, one building a real three-dimensional network with X–X bonds and another with a two-dimensional layered character. This is supported by the behavior of the lattice constants with respect to different A components. The substitution of Ca by larger Sr or Ba leads to longer a axis in the compounds with short X–X distances, whereas in the second branch the MX_4 tetrahedra are remarkably rigid. Here the substitution causes a drastic increase of the interlayer distance without changing the atomic distances within the layers. This emphasizes the distinct layer character of this $ThCr_2Si_2$ structure branch.

A remarkable trend is observed in the evolution of the interlayer X–X distances by changing the transition metal. They decrease strongly on going from the left to the right-hand side of the periodic system. In Table 1 the P–P distances of some first and second row transition metal phosphides are listed. The trend is obvious: the P–P distances decrease while filling the transition metal d shell when A remains unchanged (columns in Table 1). On the other hand, keeping the same transition element and increasing the size of the base metal atom A which separates the layers results in a significant increase of the interlayer P–P distance (rows in Table 1).

[2] Except for $LaRh_2P_2$, which adopts the related $CaBe_2Ge_2$ structure without P–P contacts (24).

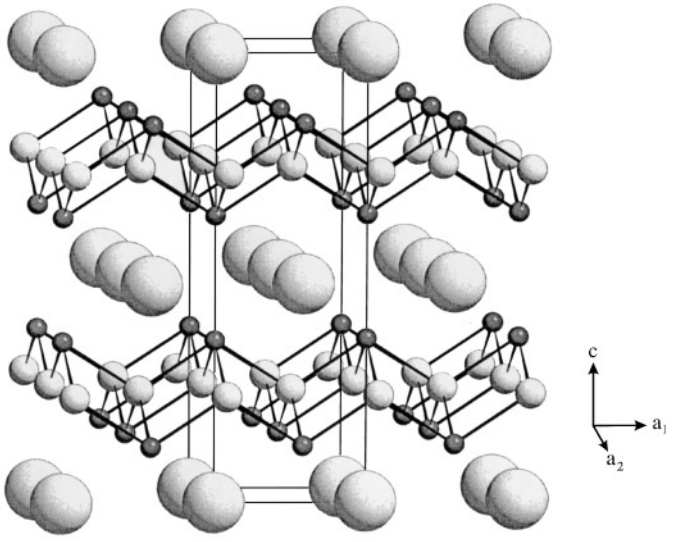

FIG. 1. The $ThCr_2Si_2$ structure: large spheres, A(Sr); medium spheres, M(Rh); small spheres, X(P).

The transition from isolated P atoms ($d_{P-P} \geqslant 3.5$ Å) to covalent P–P dumbbells ($d_{P-P} \approx 2.2$ Å) along a row in the periodic table cannot be explained by geometric reasons. Therefore, electronic factors should be a driving force for the observed interlayer distances. Based on Extended Hückel band calculations, Zheng and Hoffmann (21) drew the conclusion that the higher Fermi level of earlier transition metals causes an increased population of X–X antibonding states and longer X–X distances, respectively, which is in agreement with the observed trend. However, in this approach the X–X bonding is considered apart from the M–P interacting framework and the influence of the A element as well as the evidence of metal–metal bonding in these solids are not taken into account.

TABLE 1
Interlayer P–P Distances of $ThCr_2Si_2$-Type Phosphides [Å]

Compound	A = Ca	A = La	A = Sr	A = Ba	Ref.
AFe_2P_2	2.710	3.176	3.434	3.842	(3, 18)
ACo_2P_2	2.454	3.155	3.424	3.7[a]	(3, 18)
ANi_2P_2	2.297	2.497	3.120[b]	3.709	(3, 26, 19)
ARu_2P_2	2.576	3.004	3.271	3.7[a]	(27, 11)
ARh_2P_2	2.255	[c]	3.284	3.738	(28)
APd_2P_2	2.166	2.4[d]	2.217	2.399[e]	(29, 20)

[a] Unknown, but likely larger than 3.7 Å.
[b] $T = 100°C$.
[c] $LaRh_2P_2$ adopts the related $CaBe_2Ge_2$-type structure.
[d] P–P distance not determined, but likely smaller than 2.4 Å.
[e] $BaPd_2P_2$ adopts the related $CeMg_2Si_2$-type structure.

COMPUTATIONAL METHODS

The band structures were calculated using density functional theory with the local density approximation (LDA). The one-electron Schrödinger equation was solved self-consistently using the linear muffin-tin orbital (LMTO) method in the atomic spheres approximation (ASA) including the combined correction (CC) (30–33). This method splits the crystal space into overlapping atomic spheres whose radii were chosen to fill the crystal volume completely. The one-electron potential entering the Schrödinger equation is a superposition of overlapping spherical potential wells plus a kinetic-energy error proportional to the relative overlap of the spheres. The ASA spheridizes the charge density inside the spheres and neglects the charge outside them. This would cause substantial errors due to large sphere overlap and misrepresentation of the potential. Therefore, it is necessary to fill the interstitial space with empty spheres. In general, the requirements for choosing atomic and empty spheres radii are that the superposition of the spherical potentials approximate the full three-dimensional potential as well as possible, that the overlap-error be acceptable, and that the entire charge be inside the spheres; i.e., the sum of the spheres volumes (atomic plus empty spheres) must be equal to the unit cell volume. The atomic spheres radii and empty spheres positions and radii were calculated using an automatic procedure developed by Krier *et al.* (34). We allowed an overlap of 15% for atom centered spheres, 20% for interstitial with atomic, and 25% between empty spheres. Positions and radii of the spheres used in our calculations are summarized in Table 2. The experimental geometries of $SrRh_2P_2$, $CaRu_2P_2$, and $LuNi_2B_2C$ (35) are used as follows: Space group $I4/mmm$ (139), the A element at the position $2a(0,0,0)$, M at $4d(\frac{1}{2},0,\frac{1}{4})$, and X at $4e(0,0,z)$. The positions of the empty spheres (E–$E2$) are calculated to $2b(0,0,\frac{1}{2})$ for E, $4e(0,0,z)$ for $E1$. For $SrRh_2P_2$ the position of $E2$ is $16m(x,x,z)$ and for $LuNi_2B_2C$ $16n(x,0,z)$.

TABLE 2
Structural Data and ASA Radii Used in the LMTO Calculations

	$SrRh_2P_2$[a]	$CaRu_2P_2$[b]	$LuNi_2B_2C$
a [Å]	3.937	4.046	3.464
c [Å]	11.713	9.771	10.631
z/c (X)	0.3598	0.3682	0.3618[c]
A [a.u.]	4.19	4.14	3.62
M [a.u.]	2.53	2.48	2.59
X [a.u.]	2.47	2.38	1.54/1.56[d]
E [a.u.]	1.02	—	—
z/c	0.5		
$E1$ [a.u.]	1.00	—	1.17
z/c	0.2083		0.2129
$E2$ [a.u.]	0.95	—	0.90
x/a	0.2215		0.1667
z/c	0.1775		0.1045

[a] Also used for "KRh_2P_2," "$LaRh_2P_2$," "$SrRu_2P_2$," and "$SrPd_2P_2$."
[b] Also used for "$CaRh_2P_2$" and "$CaPd_2P_2$."
[c] The additional carbon in $LuNi_2B_2C$ is isolated at $2b$ $(0,0,\frac{1}{2})$.
[d] Values for boron/carbon.

All reciprocal space integrations were performed with the tetrahedron method (36) using 185 irreducible k points within the Brillouin zone. The basis sets consisted of 4s, 4p, and 3d orbitals for Ca and Ni; 6s, 6p, 5d, and 4f for La and Lu; 5s, 5p, and 4d orbitals for Rh, Ru, Pd, and Sr; 3s and 3p orbitals are used for P; 2s and 2p for B and C. The 3d orbitals for P and 4f for Rh, Ru, Pd, and Sr were "downfolded" using Lowdin's technique (37).

RESULTS

1. Electronic Structure of $SrRh_2P_2$

1.1. Energy bands and density of states. The calculated band structure of $SrRh_2P_2$ is shown in Fig. 2 for the Bloch vector $\mathbf{k}$ along the lines $Z = (0,0,\pi/c)$ to $\Gamma = (0,0,0)$ to $X = (\pi/a, \pi/a, 0)$ to $Z' = (2\pi/a, 0, 0)$ and back to $\Gamma = (0,0,0)$. Because of the body-centered space group, the Z point is equivalent with Z' at the top/bottom of the neighboring brillouin zones. The energy zero is taken at the Fermi level. All band structures are projected onto orthonormal partial waves. Each band is given a "width" proportional to the weight of the corresponding orthonormal orbitals. A pure band state, i.e., a 100% "fatband" is given a width of 2.5% of the energy scale, here 0.4 eV.

Several bands cross the Fermi level, in agreement with the metallic properties of $SrRh_2P_2$ (38). The two lowest lying bands around -12 eV arise from the P 3s orbitals, well separated from the states with mainly P 3p character between -4 and -7 eV. The energy range from -6 eV to the Fermi level is dominated by the 10 Rh 4d bands, which are strongly hybridized with the P 3p states, indicating strong Rh–P bonding. The transition metal atoms are surrounded tetrahedrally by four P atoms, but the RhP_4 tetrahedra are rotated by 45° around the z axis with respect to the standard setting of ligand field splitting, leading to an exchange of the d_{xy} and $d_{x^2-y^2}$ orbitals. A clear separation in energy of the d orbitals in a lower e (xy, $3z^2-1$) and higher t_2 (x^2-y^2, yz, xz) set is not seen. Nevertheless, the difference of the e and t_2 set is discerned in Fig. 2. The t_2 orbitals (Figs. 2c–2d) interact more with the P 3p orbitals than the e (Figs. 2a–2b), leading to purer fatbands for $4d_{3z^2-1}$ and $4d_{xy}$. Particularly, the $4d_{xz,yz}$ orbitals with their lobes pointing directly toward the P atoms at the vertices of the tetrahedra show strong hybridization with the P $3p_{x,y}$ (Figs. 2d and 2f).

The total density of states $N(\varepsilon)$ is shown in Fig. 3. As mentioned above, the P 3s part extends from -12.8 to -10.7 eV, followed by the lower P 3p beginning at -7 eV

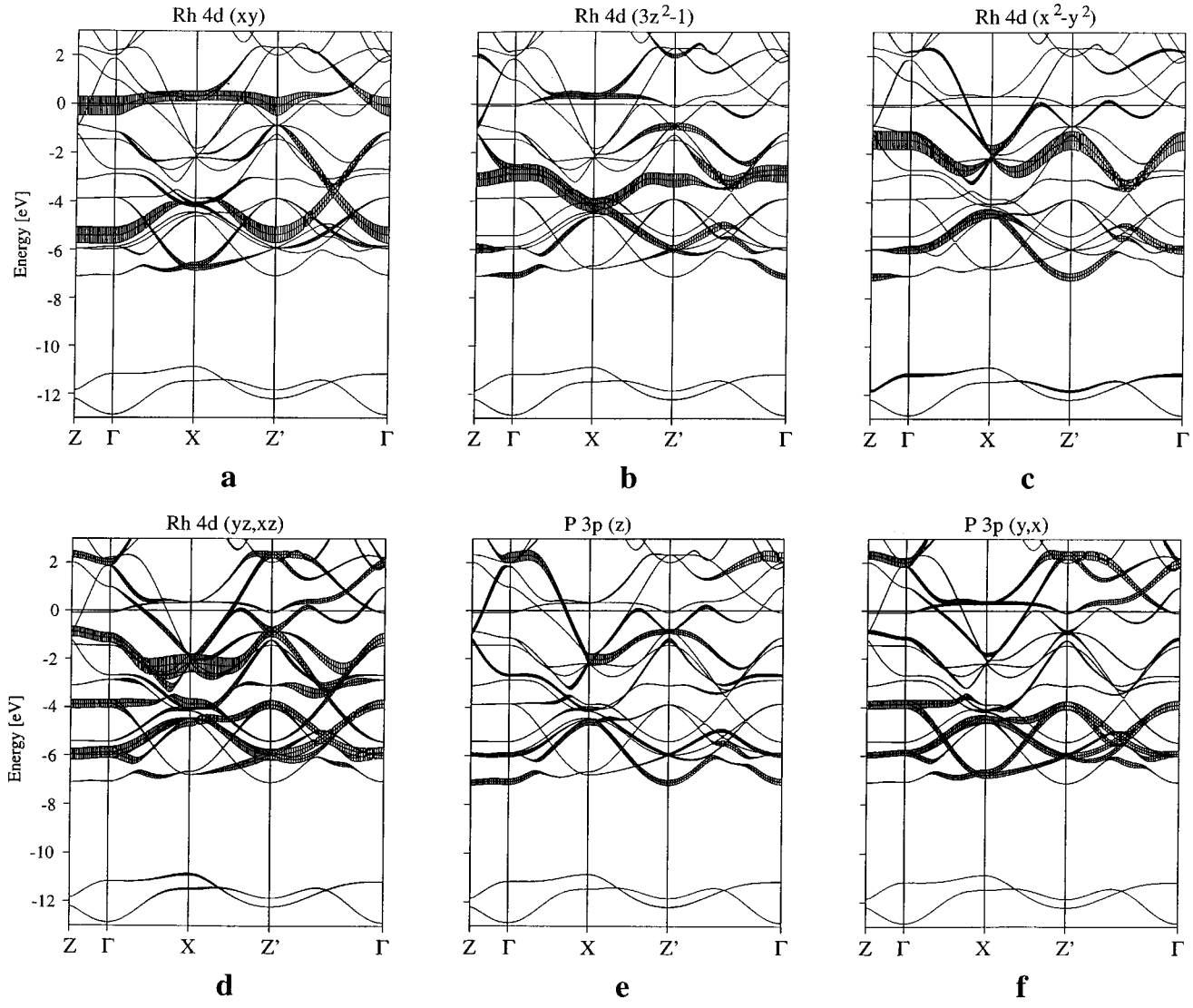

FIG. 2. Band structure of $SrRh_2P_2$ decorated with "fatbands".

and the Rh 4*d* bands extending from -6 eV up to the Fermi level. The value of the density of states at the Fermi level is $N(0) = 2.74$ states/($SrRh_2P_2 \cdot$ eV) and is composed of roughly 50% Rh 4*d*, 20% P, 20% Sr, and 10% Rh *s* and *p* states. The remarkable peak in the density of states about 0.2 eV above the Fermi level has its origin in a saddle point in the band structure at *X* (see Fig. 2a), generated mainly by the Rh $4d_{xy}$ and $4d_{3z^2-1}$ orbitals.

1.2. Rh–P bonding. The strong covalent Rh–P bonding within the $^2_\infty[RhP_{4/4}]$ layers results from the interaction of the P 3*s* and 3*p* orbitals with the symmetry matching Rh 4*d* t_2 set, hybridized with the 4*s* and 4*p* levels. The P $3p_{x,y}$ fatbands in Fig. 2f show the Rh–P bonding bands with mainly P character extending from -7 to -4 eV. The interaction of the P $3p_z$ levels with the Rh *e* set is weaker because of the smaller overlap (Figs. 2a and 2b). Above -4 eV up to the Fermi level, the P contribution is smaller. These bands correspond mainly to the crystal field destabilized Rh–P antibonding orbitals with t_2 symmetry (Figs. 2c–2d). Thus, a decreasing electron filling should enhance the metal–nonmetal bonding in this structure and vice versa.

1.3. Rh–Rh bonding. The Rh–Rh distance in $SrRh_2P_2$ is 2.78 Å, not much longer than in Rh metal with 2.69 Å. The interaction between the Rh atoms here is mainly made by the $4d_{xy}$ orbitals with their lobes pointing directly toward the Rh neighbors, as shown schematically in Fig. 4. In order to show their bonding character, we have formed the even/odd linear orbital combinations $(1/\sqrt{2})(d_{xy,\mathrm{Rh1}} +/- d_{xy,\mathrm{Rh2}})$, drawn as fatbands in Fig. 5. The bonding $dd\sigma$

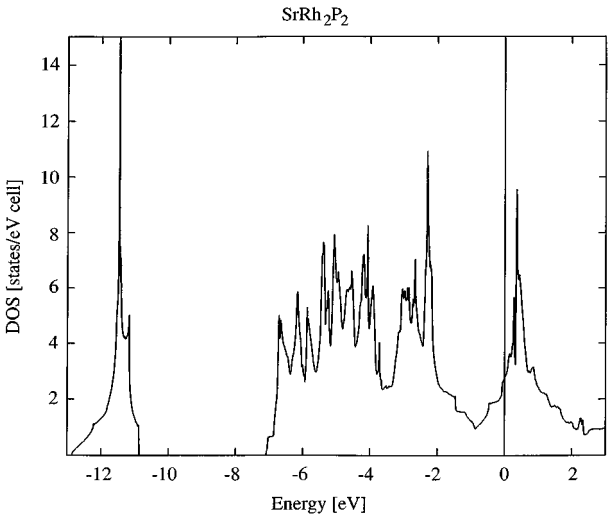

FIG. 3. Total density of states of $SrRh_2P_2$. The energy zero is taken at the Fermi level.

(Fig. 5a) and antibonding $dd\sigma^*$ (Fig. 5b) bands are split by more than 5 eV, indicating strong metal–metal interaction. As expected, their dispersion is large along Γ–X–Z' and almost zero in the Z–Γ direction, i.e., perpendicular to the Rh planes. With k going from Z' to Γ, the $4d_{xy}$ bands disperse strongly by mixing with $4d_{xz,yz}$. From Γ to X the $dd\sigma^*$ band goes up in energy due to hybridization with the $4d_{3z^2-1}$ orbital (i.e., the $dd\pi^*$, Fig. 2b) and crosses the Fermi energy. Thus, the conduction band of $SrRh_2P_2$ has mainly Rh $4d_{xy}$ character. Along X–Z' the $4d_{xy}$ contribution decreases by mixing with the $4d_{xz,yz}$ and P $3p_{x,y}$. The band is

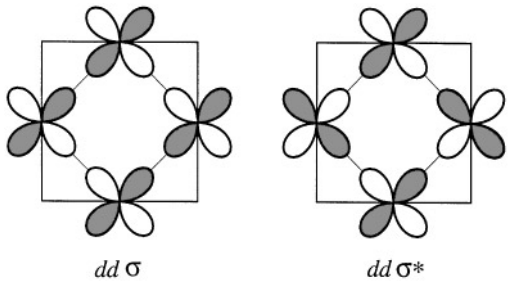

FIG. 4. Rhodium $dd\sigma$ and $dd\sigma^*$ orbitals (schematic).

pushed up in energy, since this orbital combination has Rh–P antibonding character. A saddle point of the $dd\sigma^*$ band at X leads to a hyperbolic behavior of the energy surface $\varepsilon(k)$, since the lines Γ–X and X–Z' have orthogonal directions in the reciprocal space. The saddle point is about 0.2 eV above the Fermi level, which is indicated by the sharp peak in the density of states (Fig. 3).

In $SrRh_2P_2$, the Rh–Rh antibonding band is approximately 30% filled so substantial metal–metal bonding is present. This may be strongly decreased by adding more electrons or increased by reducing the electron count. The metal–metal bonding vanishes if the $dd\sigma^*$ band is completely filled, i.e., when the Fermi energy increases above the saddle point.

1.4. P–P bonding. The interlayer P–P distance in $SrRh_2P_2$ is 3.28 Å, so the interaction of the P atoms is expected to be small and, if any, limited to the P $3p_z$ orbitals. As for the Rh–Rh bonding in the previous section, we have separated the P–P bonding band states $pp\sigma$ from the

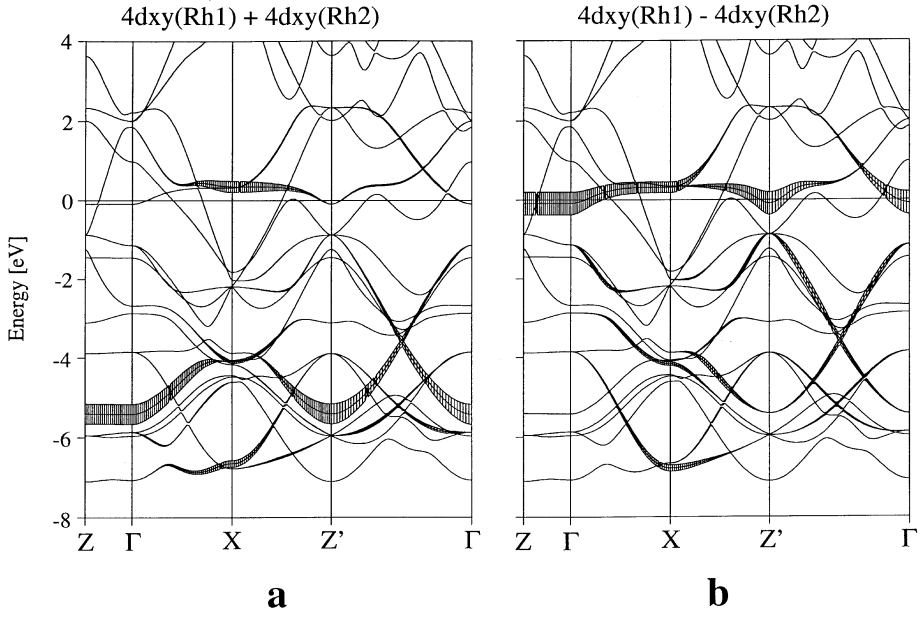

FIG. 5. Fatband representation of the rhodium $dd\sigma$ and $dd\sigma^*$ linear combinations.

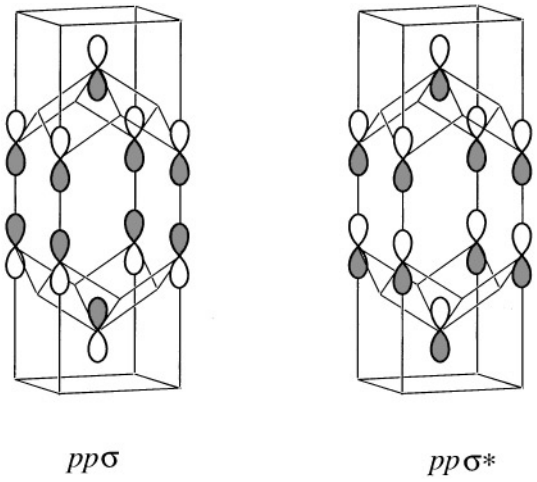

FIG. 6. Phosphorus $pp\sigma$ and $pp\sigma^*$ orbitals (schematic).

antibonding $pp\sigma^*$ by forming the linear combinations $(1/\sqrt{2})(p_{z,\mathrm{P1}} +/- p_{z,\mathrm{P2}})$. The corresponding p_z orbitals are depicted schematically in Fig. 6; the resulting fatbands are shown in Fig. 7. We find most of the bonding states around -6 eV (Fig. 7a), but there is additional $pp\sigma$ character within some metal-centered bands. Particularly, the band touching the Fermi level between X–Z' and Z'–Γ (Fig. 7a) is important. It is generated by the Rh–P antibonding interaction which increases the energy of a P–P bonding $3p_z$ orbital combination and places it in the vicinity of the Fermi level. In this way, the P–P bond becomes dependent on the electron count. Since this band has P–P bonding and M–P antibonding character (P–P $pp\sigma$, M–P $dp\sigma^*$), its energy depends strongly on the metal–phosphorus interaction. This is also the case for the $pp\sigma^*$ levels along Γ–X in Fig. 7b. The highest energy is reached at the Γ point, because this orbital combination is Rh–P and P–P antibonding here. At X we find less metal character; i.e., the energy of this $pp\sigma^*$ state here is mainly determined by the atomic distance.

The P–P $pp\sigma$ M–P $dp\sigma^*$ band in the vicinity of the Fermi level is almost filled in $SrRh_2P_2$ (see Figs. 7a and 7b). Frozen phonon calculations show that it is very sensitive to small atomic displacements. By decreasing the z parameter of P by 0.005 (i.e., about 0.06 Å), this band is partly pushed above the Fermi level, leading to an increased filling of $dd(\sigma,\pi)^*$ levels along Γ–X and to weaker metal–metal bonds. This remarkable sensitivity indicates strong electron–phonon coupling in this structure and may be responsible for instabilities resulting in phase transitions or lattice distortions. Indeed, we have observed phase transitions in $SrRh_2P_2$, $SrRh_2As_2$ (39), $EuRh_2P_2$, and $SrNi_2P_2$ (40) with drastic changes of the P–P distances. In all of these compounds, we find this band to be touching E_F. Along the symmetry line Γ–Z, corresponding to the direct P $3p_z$ interaction, we find four bands with P $3p_z$ orbital contribution because of their hybridization with the Rh $4d_{x^2-y^2}$ and $4d_{3z^2-1}$, i.e., the Rh e set. This leads to the following order in energy at Γ and Z: $[\sigma_{\mathrm{P-P}}\,\sigma_{\mathrm{Rh-P}}]$ at -7 eV, $[\sigma^*_{\mathrm{P-P}}\,\sigma_{\mathrm{Rh-P}}]$ at -6 eV, $[\sigma_{\mathrm{P-P}}\,\sigma^*_{\mathrm{Rh-P}}]$ at -2 eV, and $[\sigma^*_{\mathrm{P-P}}\,\sigma^*_{\mathrm{Rh-P}}]$ around

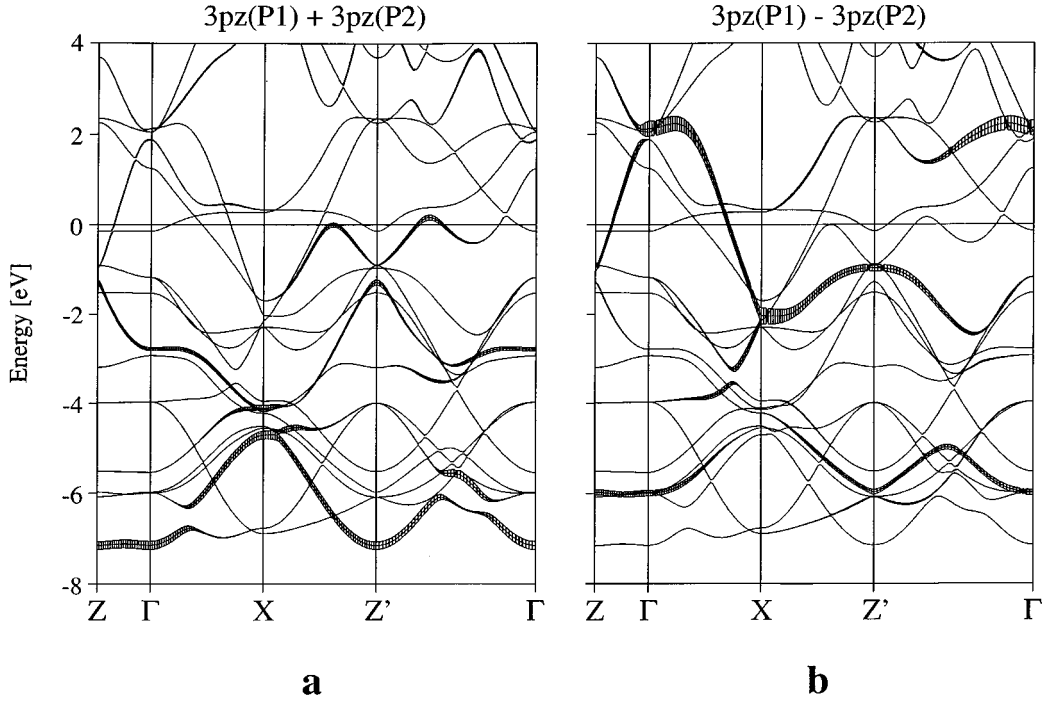

FIG. 7. Fatband representation of the phosphorus $pp\sigma$ and $pp\sigma^*$ linear combinations.

0 eV cutting the Fermi level. Again the Rh–P interaction determines the position of the P $3p_z$ bands in energy, otherwise the bonding character of the second and third band would be exchanged.

Although the P–P distance is long in $SrRh_2P_2$, we have little bonding interaction between them, rather than a real lone pair behavior. Otherwise, we should find a smaller splitting between the $pp\sigma$ and $pp\sigma^*$ levels and both below the Fermi level. This is realized here around the X point, where the metal contribution is small. Particularly, along X–Γ, $pp\sigma^*$ levels are pushed up over the Fermi level by the additional Rh–P antibonding character. Thus, the presence of the strong Rh–P interaction leads to weak interlayer P–P bonding in $SrRh_2P_2$.

2. The Effects of Substitution

The electronic states around the Fermi energy in $SrRh_2P_2$ have antibonding character with respect to the Rh–P and Rh–Rh bonds. Therefore, any decrease of the electron count should enhance the bonding and hence the stability of this structure. One possibility is the substitution of the base metal component (A), e.g., the divalent Sr by monovalent alkaline metal or, in the other direction, by trivalent La. A look at the experimental data shows that this generally has no strong influence on the bonding distances within the $^2_\infty[MX_{4/4}]$ layers and the changes of the c axis are rather due to the different radii of A. In contrast to this, a variation of the transition metal component (M) leads to drastic changes of the P–P interlayer bonding and small differences in the M–M and M–P distances.

In order to study only the influence of substitution on the electronic structure, we have calculated the band structures of some isostructural compounds, using the geometry of $SrRh_2P_2$ with K and La instead of Sr and with Ru and Pd instead of Rh. To investigate the observed trend in the interlayer P–P bonding in more detail, we present also the band structure of $CaRu_2P_2$ and substitute Ru by Rh or Pd.

2.1. Changing the base-metal component (A). The band structures of "$LaRh_2P_2$," $SrRh_2P_2$, and "KRh_2P_2" are shown in Fig. 8, decorated with the fatbands for K 3d, Sr 4d, and La 5d orbitals, respectively. No significant Sr 4d contribution is found below the Fermi energy; i.e., Sr is nearly in the divalent state. Surprisingly, the Fermi level is nearly the same for the La substituted compound compared with $SrRh_2P_2$. As seen from the fatband structure in Fig. 8c, the La $5d_{x^2-y^2}$ level is substantially populated. This is the reason for the almost constant Fermi energy. Thus, the substitution of Sr by La would have nearly no influence on bonding in this structure and geometric effects regarding the smaller atomic radii of La may be of greater influence. Nevertheless this is an important result. Since the La d shell is partially occupied, we have La^{2+} rather than La^{3+} in this structure. This indicates some covalent La–La interaction, but since the La–La distances are about 4.0 Å, this bonding is extremely weak and therefore neglected here. We suppose that this holds for the other lanthanoid elements, particularly for the heavier ones with lower lying d orbitals.

In contrast to this, no potassium 3d states are found below E_F. This means that K is almost fully ionized to K^+ and the Fermi level for "KRh_2P_2" is reduced by more than 1 eV, resulting in a depopulation of Rh–P and Rh–Rh antibonding states (Fig. 8a). The metal–metal bonding is more enhanced because the antibonding $4d_{xy}$ band is now completely empty. This is in good agreement with the real

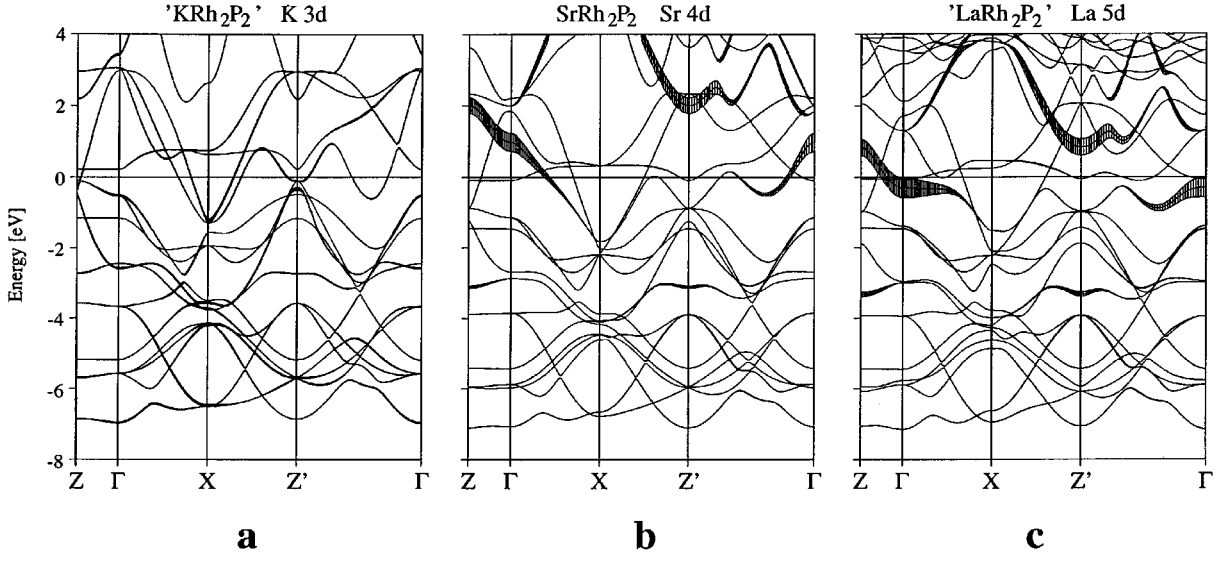

FIG. 8. Band structures of "KRh_2P_2" and "$LaRh_2P_2$," compared with $SrRh_2P_2$. The d levels of the A component are drawn as fatbands.

structure of KRh_2P_2 (41). The *a* axis and therefore the Rh–Rh bond is shorter compared with $SrRh_2P_2$, although the radius of potassium is greater than that of strontium. This is compensated by an increase of the *c* axis by 1.2 Å, which also confirms our result that the $^2_\infty[RhP_{4/4}]$ layers themselves become more rigid when the band filling is decreased.

2.2. Changing the transition metal component (M). As mentioned above, one of the most interesting features of the $ThCr_2Si_2$-type compounds is the enormous variety of the interlayer *X–X* distances. According to Zheng and Hoffmann, this is due to a depopulation of P–P antibonding levels by the decreasing transition metal Fermi level. The conclusion was drawn on the basis of Extended Hückel band calculations for a $(Mn_2P_2)^{2-}$ fragment structure. We have calculated the band structures of "$SrRu_2P_2$" and "$SrPd_2P_2$"; i.e., we substitute Rh in $SrRh_2P_2$ by the left and right transition metal neighbors, keeping the geometry of the Rh compound in order to see only the electronic effect. The band structures decorated with the P $3p_z$ fatbands are shown in Fig. 9. They do not reproduce the result of Zheng and Hoffmann. The LMTO calculation reveals that the occupation of the strong P–P antibonding bands ($pp\sigma^*$, in particular along Γ–*X*, see Fig. 7b) would be higher for Palladium than for Ruthenium. This means that the reason for $SrPd_2P_2$ to form a P–P distance of 2.2 Å instead of 3.3 Å as $SrRh_2P_2$ or $SrRu_2P_2$ cannot be the depopulation of P–P antibonding states due to the decreasing energy of the *d* levels.

All band structures discussed here so far belong to the $ThCr_2Si_2$-type branch forming long interlayer *X–X* distances; i.e., the interactions between the P $3p_z$ orbitals are weak. To study the evolution of the interlayer bond lengths with different transition metals in more detail, representatives with shorter P–P distances are more appropriate. We chose the CaM_2P_2 compounds with *M* = Ru, Rh, and Pd forming P–P distances of 2.58, 2.26, and 2.17 Å, i.e., much smaller than for the Sr analogues (Table 1). From this it appears also that the transition metals from the left side of the periodic system tend to form longer P–P distances. We have calculated the band structures of $CaRu_2P_2$, "$CaRh_2P_2$," and "$CaPd_2P_2$" each using the geometry of the Ruthenium compound, fixing the P–P distance to 2.58 Å. Figures 10a–10c show the band structures with the P $3p_z$ fatbands.

The energy of the strong P–P $pp\sigma^*$ band at the *X* point is much higher now compared with that in $SrRh_2P_2$. This is as expected, since there is no substantial metal contribution; i.e., the position of this level is mainly a function of the geometric P–P separation. However, this band is not occupied in all three compounds, therefore it cannot be responsible for the trend in the distances. Starting with the Ru compound (Fig. 10a), the additional electrons occupy mainly metal centered levels. Particularly, the metal–metal antibonding $dd(\sigma,\pi)^*$ band is empty for Ru, partially filled for Rh and completely occupied in the Pd case. Hence, the

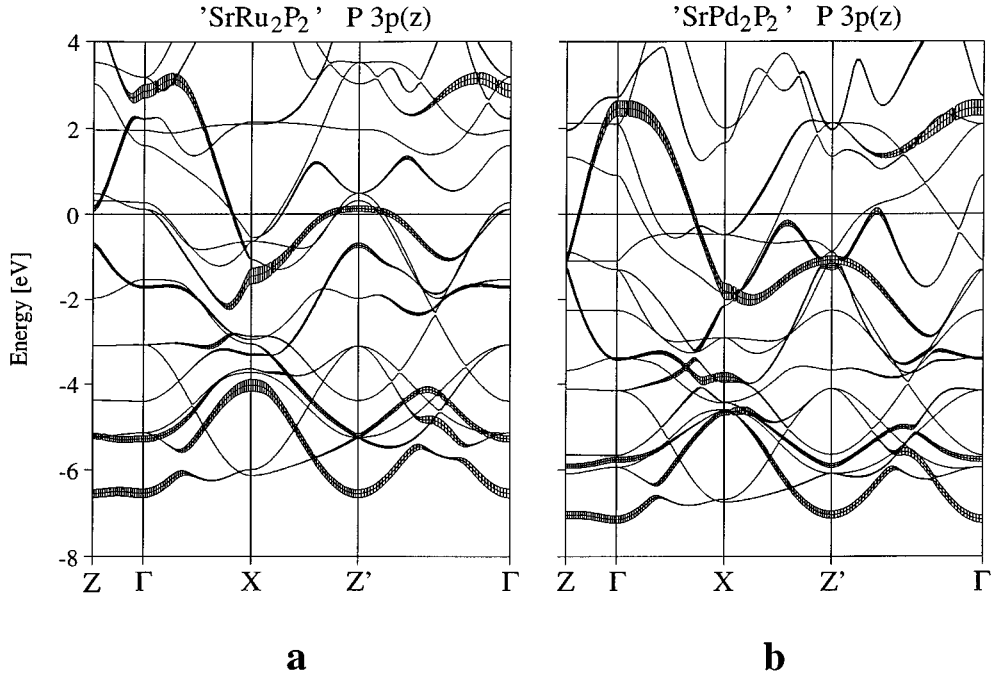

FIG. 9. Band structures of "$SrRu_2P_2$" and "$SrPd_2P_2$" decorated with the P $3p_z$ fatbands.

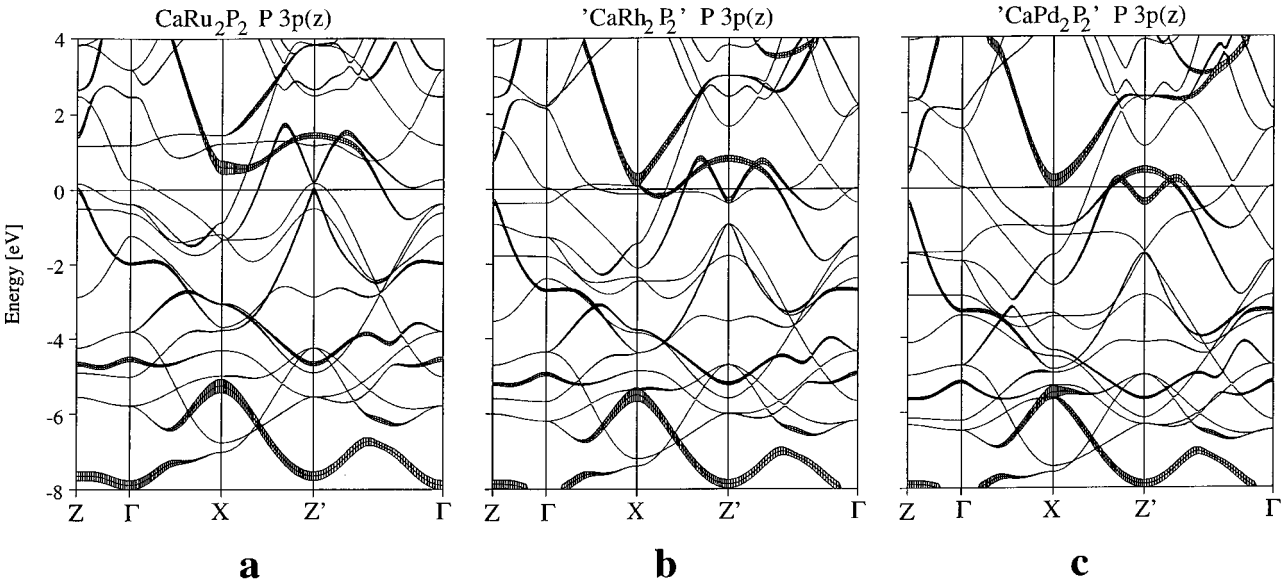

FIG. 10. Band structures of $CaRu_2P_2$, "$CaRh_2P_2$," and "$CaPd_2P_2$," decorated with the P $3p_z$ fatbands.

metal–metal bonding decreases strongly with band filling and is no longer present in the Palladium compound.

The band extending from the Fermi level at Z' to $+1$ eV along X–Z'–Γ (Fig. 10a) is filled successively on going from Ru to Pd and at the same time the P $3p_z$ character increases (Figs. 10b and 10c). As discussed in Section 1.4, the composition of this band is relatively complex, but basically it is antibonding for the M–P and bonding for the P–P interaction, respectively (see Fig. 7b). When the d orbital energy goes down, this band becomes more $pp\sigma$, i.e., exhibits more P–P bonding character. Filling this band weakens the metal–nonmetal bonds within the tetrahedral layers but favors the formation of interlayer P–P bonds. Furthermore, the antibonding character of the band along Z–Γ around -4.5 eV decreases slightly, since it has more metal character when the d orbital energy is lower.

This situation is schematically depicted in Fig. 11. Due to the M–P antibonding interaction ($dp\sigma^*$), the highest occupied levels have P–P bonding ($pp\sigma$) character. Any additional electron leads, therefore, to shorter P–P bonds. With lower d orbital energies this effect increases, since the metal character of this band decreases. Furthermore, the lower lying $dp\sigma/pp\sigma^*$ band becomes less antibonding when the d orbital energy goes down.

Now we can explain the discrepancies in bonding within the $ThCr_2Si_2$ family from the electronic structure viewpoint. The increasing d band occupation on going from left to right in the periodic system leads to weaker M–M and M–P bonds and therefore the layers becomes less rigid within the a_1a_2 plane. This is in agreement with the experimental observation that for the compounds with filled d shells like copper or palladium, the a-lattice constants increase substantially with the radii of the base metal atoms. A larger metal–metal separation inevitably causes a shortening of the interlayer distances for geometric reasons: The transition metal planes (and so the MX_4 tetrahedra) are separated in the z direction by the base metal atoms A; therefore, this distance must decrease by widening the metal squares in order to maintain the A–M contacts. At the same time, the formation of interlayer P–P bonds is favored by filling the $pp\sigma$ bonding states at the top of the metal d band and weakening the antibonding character of the low lying

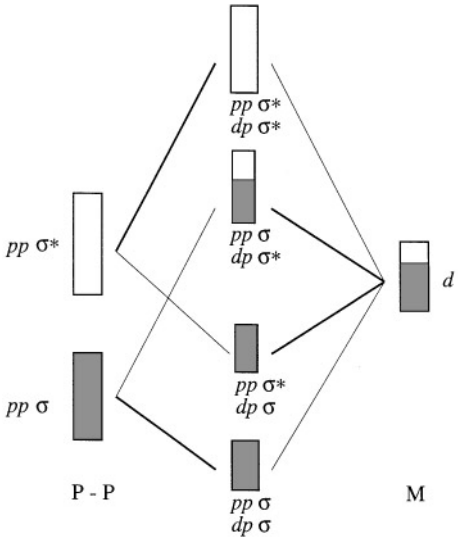

FIG. 11. Interaction scheme of the nonmetal $pp\sigma$ and $pp\sigma^*$ orbitals with the transition metal d orbitals.

$pp\sigma^*/dp\sigma$ band. The latter effect is weak here but plays an important role in chalcogen compounds; e.g., the S–S distance in transition metal pyrites has been said to be determined by this (42, 43). The reason is the substantial lower orbital energy of sulphur compared with phosphorus.

Hence, the formation of X–X bonds in the $ThCr_2Si_2$ structure is controlled by the transition metal d orbitals, but in a way different from what was stated previously (21). What we find here is not the depopulation of antibonding but the population of X–X bonding states accompanied by a weakening of the intralayer bonds, leading to geometric conditions favorable for shorter P–P distances. Two effects are working toward shorter P–P bonds on going from left to right in the periodic system and it is clear now that the variety of the interlayer P–P distances must be much larger than the changing of the M–P bonds. It is not reasonable to separate the P–P bond from the metal–metal and metal–nonmetal interactions since there are strong electronic dependencies. At long last, our result is a proof again of the principle that any compound tends to find an optimal balance among all bonding interactions.

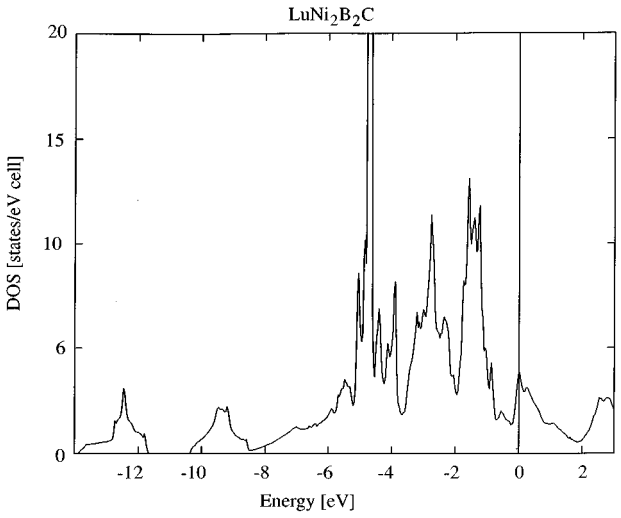

FIG. 12. Total density of states of $LuNi_2B_2C$. The energy zero is taken at the Fermi level.

3. *Superconductivity in $ThCr_2Si_2$-Type Compounds*

Despite the large number of $ThCr_2Si_2$-type compounds, superconductivity has been observed scarcely and mainly at very low temperatures. In contrast to this, the discovery of transition temperatures up to 23 K in the related boron carbides with a linear B–C–B unit instead of the P–P dumbbell is surprising. The electronic structure of this system has been studied intensively by several groups (15–17). Nevertheless we have recalculated the band structure of $LuNi_2B_2C$ in order to compare its main features with our results on the phosphides and try an approach to the question of which conditions may favor the occurrence of superconductivity.

The density of states for $LuNi_2B_2C$ are shown in Fig. 12. Here the peak in the DOS nearly coincides with the Fermi level. The value of the DOS at the Fermi energy is calculated to $N(0) = 3.9$ states/eV · cell and composed of roughly 70% Ni 3d and 10% each of C 2p, B 2p, and Lu 5d orbitals, respectively. Such a DOS peak close to the Fermi level is also found in $YBa_2Cu_3O_7$ (44) as well as in the A15 superconductors (45). Figure 13 shows the band structure of $LuNi_2B_2C$, projected on the Ni–Ni antibonding $dd\sigma^*$ and

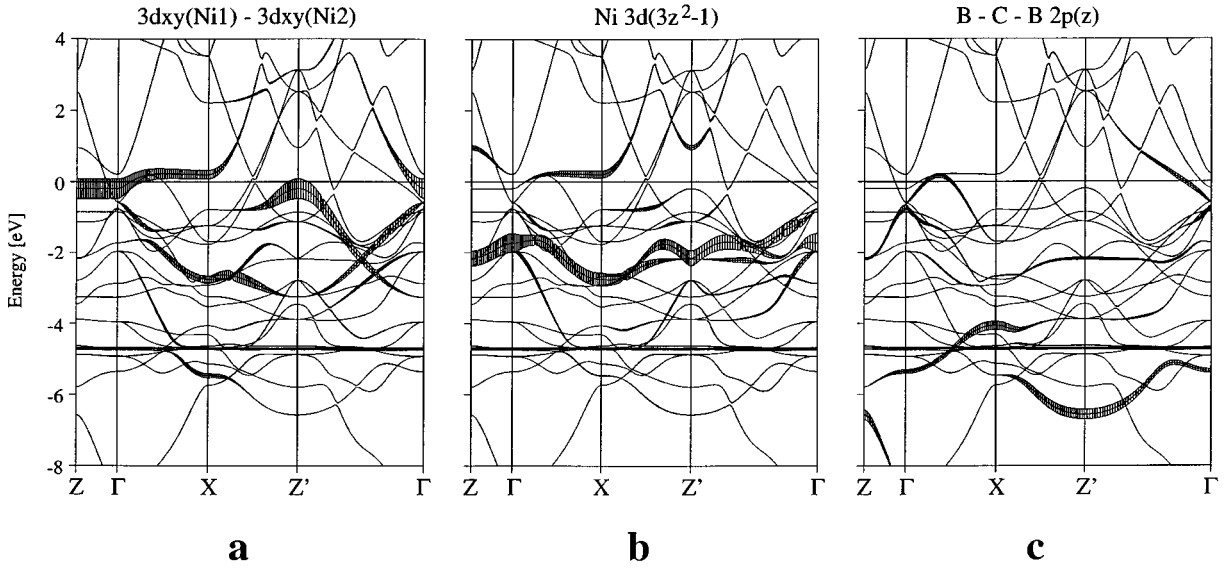

FIG. 13. Band structure of $LuNi_2B_2C$ projected on the Ni $dd\sigma^*$, $dd\pi^*$, and B–C–B $pp\sigma$ linear combinations.

$dd\pi$* orbitals (Figs. 13a and 13b) and the B–C–B bonding $ppp\sigma$ linear combinations (Fig. 13c). It is well established that the bands around E_F are responsible for superconductivity. Here we find three bands cutting the Fermi level, but only one leads to the DOS peak. As described in Section 1.3 for $SrRh_2P_2$, the hybridization of the Ni d_{xy} and d_{z^2} leads to a saddle point in the energy surface, i.e., a van Hove singularity at X. Along Z–Γ we find 100% $dd\sigma$* band states without any dispersion. At the X point, this band is composed roughly of 85% Ni, 10% Lu, and 5% B orbitals. Since the dispersion in the Z direction is zero and the main contributions are from the Ni $dd(\sigma,\pi)$* orbitals, this band has substantial 2D character. Furthermore, only this 2D band is responsible for the DOS peak and in our opinion therefore plays an important role for superconductivity, although the overall electronic structure is described to be 3D (15).

In contrast to the Rh compound (see Fig. 4b), the Ni–Ni bonding band is below the Fermi level along Z'–X due to small hybridization with the Carbon 2p, indicating a charge transfer to the transition metal. A second metal-centered band crosses the Fermi level and touches the "singularity band" between Γ and X. This is generated by the interaction of the Ni $3d_{x^2-y^2}$ with the B–C–B bonding p_z orbital combination (Fig. 13c). The third band cutting the Fermi energy has pure Lu $5d_{x^2-y^2}$ character, forming a small electron pocket at Γ. Again the Lutetium is not fully ionized to the trivalent state.

The only superconducting phosphide with $ThCr_2Si_2$ structure is $LaRu_2P_2$ with $T_c = 4.1$ K. In this compound, the transition-metal d shell is only partially filled and so the antibonding $dd(\sigma,\pi)$* bands are well above the Fermi level, which is crossed by higher dispersed bands exclusively. Hence, no large peak in the DOS and no saddle point in the band structure are observed at the Fermi energy. In our opinion, $LaRu_2P_2$ as well as the other superconducting $ThCr_2Si_2$ compounds with low T_c are conventional BCS superconductors, whereas $LuNi_2B_2C$ can be discussed within the framework of the van Hove singularity scenario (46). The isotope shift of the Ni atoms could be a good possibility to prove this. Superconductivity in $LuNi_2B_2C$ seems to be unlike to that in the copper oxides but similar to that in the A15 compounds, because here the bands generated by metal–metal bonding play likewise an important role.

There are however, striking similarities in the electronic structures of $LuNi_2B_2C$ and nonsuperconducting $SrRh_2P_2$, particularly regarding the metal–metal bonding. Reasons for the lack of superconductivity (above 2 K) could be the fact that the DOS peak is about 0.2 eV above the Fermi level and/or the smaller dispersion of the $dd(\sigma,\pi)$* band in the Rh compound. Small doping of the transition metal in $LuNi_2B_2C$ has shown that T_c and the position of the DOS peak depend strongly on the impurity concentration (47, 48). Furthermore, the absence of the second band with the nonmetal p_z contribution may be important.

CONCLUSION

The LMTO calculations reveal a detailed picture of an exceptional bonding situation within the $ThCr_2Si_2$-type compounds. Neither a covalent nor ionic or metallic bonding scheme alone can give an appropriate description here. In fact, all three kinds of bonding are present in these materials, with mutual dependencies. So this system is very flexible in its electronic structure, which may be one reason for the great "success" of the $ThCr_2Si_2$ type, i.e., the unique number of representatives.

Despite the overall metallic character, we find strong covalent M–X bonding within negative polarized ${}^2_\infty[MX_{4/4}]^{\delta-}$ layers, attracted by the ionized $A^{\delta+}$ atoms. Interlayer bonding between the X atoms, if possible by geometry, is controlled by the transition metal d shell. X–X $pp\sigma$ bonding states are pushed up to the vicinity of the Fermi level by the antibonding M–X interaction. For this reason, an increasing band filling results in weaker bonds within the layers, whereas the formation of covalent bonds between them becomes favored.

Metal–metal bonding plays an important role in the $ThCr_2Si_2$ structure and influences indirectly the X–X distances. When the transition-metal d shell gets completely filled, the attractive metal–metal interaction vanishes and the distance is elongated. As a consequence of the larger metal squares, the interlayer distance becomes smaller for geometric reasons and the X–X interaction gets stronger again.

The role of the base metal component A, besides its electron donor function, is primarily a geometric one. Very electropositive metals like alkaline and alkaline–earth elements are almost completely ionized in these structures. In contrast, the lanthanides are found not to be in the expected trivalent state since their d shells become partially occupied.

All results are in good agreement with the experimental data regarding structural pecularities, effects by changing electron counts, as well as lattice instabilities leading to phase transitions.

Superconductivity in the "filled" $ThCr_2Si_2$ structure of $LuNi_2B_2C$ is described to be BCS-like so far. The authors drew this conclusion from the composition of the DOS at E_F. Contributions from all atoms are present here, indicating 3D metallic character of the overall electronic structure. In contrast to this, we suppose the important factor for superconductivity here is the metal–metal antibonding band with substantial 2D character, generating a van Hove singularity near the Fermi level. Assuming this to be an essential electronic factor for superconductivity, it should be possible to induce it in $SrRh_2P_2$ or related compounds by doping with Ni, Pd, or La. Furthermore, the influence of the

additional carbon is not yet clear. The preparation of corresponding phosphides with an interstitial carbon or boron could be a way to study this.

ACKNOWLEDGMENTS

We thank the Deutsche Forschungsgemeinschaft, the Region des Pays de Loire (France), and the Fonds der Chemischen Industrie for financial support.

REFERENCES

1. Z. Ban and M. Sikirica, *Acta Cryst.* **18,** 594 (1965).
2. P. Villars and L. D. Calvert, "Pearson's Handbook of Crystallographic Data for Intermetallic Phases," second ed. ASM International, Materials Park, OH, 1991.
3. A. Mewis, *Z. Naturforsch. B* **35,** 141 (1980).
4. R. Nagarajan *et al.*, *Phys. Lett. A* **84,** 275 (1981).
5. G. Neumann, J. Langen, H. Zahel, D. Plümacher, Z. Kletowski, W. Schlabitz, and D. Wohlleben, *Z. Phys. B: Condens. Mat.* **59,** 133 (1985).
6. F. Steglich *et al.*, *Phys. Rev. Lett.* **43,** 1892 (1987).
7. K. A. Gschneider and L. Eyring, "Handbook of Physics and Chemistry of Rare Earth," Vol. 12. p. 133. Elsevier, Amsterdam, 1989.
8. M. Reehuis and W. Jeitschko, *J. Phys. Chem. Solids* **51,** 961 (1990).
9. E. Mörsen, B. D. Mosel, W. Müller-Warmuth, M. Reehuis, and W. Jeitschko, *J. Phys. Chem. Solids* **49,** 785 (1988).
10. M. Reehuis, W. Jeitschko, M. H. Möller, and P. J. Braun, *J. Phys. Chem. Solids* **53,** 687 (1992).
11. W. Jeitschko *et al.*, *J. Solid State Chem.* **69,** 93 (1987).
12. R. Nagarajan *et al.*, *Phys. Rev. Lett.* **72,** 274 (1994).
13. R. J. Cava *et al.*, *Nature* **367,** 252 (1994).
14. R. J. Cava *et al.*, *Phys. Rev. B* **49,** 384 (1994).
15. L. F. Mattheiss, *Phys. Rev. B* **49,** 279 (1994).
16. W. E. Pickett and D. Singh, *Phys. Rev. Lett.* **72,** 3702 (1994).
17. H. Kim, C.-D. Hwang, and J. Ihm, *Phys. Rev. B* **52,** 4592 (1995).
18. W. Jeitschko, U. Meisen, M. H. Möller, and M. Reehuis, *Z. Anorg. Allg. Chem.* **527,** 73 (1985).
19. W. K. Hoffmann and W. Jeitschko, *J. Solid State Chem.* **51,** 152 (1984).
20. W. K. Hoffmann and W. Jeitschko, *J. Less-Common Met.* **95,** 317 (1983).
21. C. Zheng and R. Hoffmann, *J. Phys. Chem.* **89,** 4175 (1985).
22. C. Zheng and R. Hoffmann, *J. Solid State Chem.* **72,** 58 (1988).
23. C. Zheng, *J. Am. Chem. Soc.* **115,** 1047 (1993).
24. R. Madar, P. Chaudouet, J. P. Senateur, S. Zemni, and D. Tranqui, *J. Less-Common Met.* **133,** 303 (1987).
25. J. Labbé and J. Bok, *Europhys. Lett.* **3,** 1225 (1987).
26. V. Keimes, D. Johrendt, and A. Mewis, to be published.
27. G. Wenski and A. Mewis, *Z. Naturforsch. B* **41,** 38 (1986).
28. A. Wurth and A. Mewis, to be published.
29. A. Mewis, *Z. Naturforsch. B* **39,** 713 (1984).
30. O. K. Andersen, *Phys. Rev. B* **12,** 3060 (1975).
31. O. K. Andersen and O. Jepsen, *Phys. Rev. Lett.* **53,** 2571 (1984).
32. O. K. Andersen, O. Jepsen, and D. Glötzel, *in* "Highlights of Condensed Matter Theory," (F. Bassani, F. Fumi, and M. P. Tosi, Eds.). North-Holland, New York, 1985.
33. O. Jepsen and O. K. Andersen, *Z. Phys. B* **97,** 35 (1995).
34. G. Krier, O. K. Andersen, and O. Jepsen, to be published.
35. T. Siegrist, R. J. Cava, J. J. Krajewski, and W. F. Pech Jr., *J. Alloys Comp.* **216,** 135 (1994).
36. O. Jepsen and O. K. Andersen, *Solid State Comm.* **9,** 1763 (1971).
37. W. R. L. Lambrecht and O. K. Andersen, *Phys Rev. B* **34,** 2439 (1986).
38. D. Johrendt, C. Felser, C. Payen, and J. Rouxel, private communication.
39. A. Wurth, A. Mewis, *et al.*, to be published.
40. V. Keimes and A. Mewis, to be published.
41. S. Rosza and H.-U. Schuster, *Z. Naturforsch. B* **36,** 1668 (1981).
42. J. C. W. Folmer, F. Jellinek, and G. H. M. Calis, *J. Solid State Chem.* **72,** 137 (1988).
43. S. Jobic, R. Brec, and J. Rouxel, *J. Alloys Comp.* **178,** 253 (1992).
44. O. K. Andersen, A. I. Liechtenstein, O. Jepsen, and F. Paulsen, *J. Phys. Chem. Solids* **56,** 1573 (1995).
45. J. Labbé and F. Friedel, *J. Phys.* (*Paris*) **27,** 153 (1966).
46. C. Felser, O. Jepsen, and O. K. Andersen, to be published.
47. Z. Zeng, D. E. Ellis, D. Guenzburger, and E. M. Baggio-Saitovitch, *Phys. Rev. B* **53,** 6613 (1996).
48. S. L. Bud'ko, M. El Massalami, M. B. Fontes, J. Mondragon, W. Vanori, B. Vierdanengo, and E. M. Baggio-Saitovitch, *Physica C* **243,** 183 (1995).